Description and evaluation of a tropospheric ozone lidar implemented on an existing lidar in the southern subtropics

Jean-Luc Baray, Jean Leveau, Jacques Porteneuve, Gérard Ancellet, Philippe Keckhut, Françoise Posny, and Serge Baldy

Rayleigh–Mie lidar measurements of stratospheric temperature and aerosol profiles have been carried out at Reunion Island (southern tropics) since 1993. Since June 1998, an operational extension of the system is permitting additional measurements of tropospheric ozone to be made by differential absorption lidar. The emission wavelengths (289 and 316 nm) are obtained by stimulated Raman shifting of the fourth harmonic of a Nd:YAG laser in a high-pressure deuterium cell. A mosaic of four parabolic mirrors collects the backscattered signal, and the transmission is processed by the multiple fiber collector method. The altitude range of ozone profiles obtained with this system is 3–17 km. Technical details of this lidar system working in the southern tropics, comparisons of ozone lidar profiles with radiosondes, and scientific perspectives are presented. The significant lack of tropospheric ozone measurements in the tropical and equatorial regions, the particular scientific interest in these regions, and the altitude range of the ozone measurements to 16–17 km make this lidar supplement useful and its adaptation technically conceivable at many Rayleigh–Mie lidar stations.

OCIS codes: 010.0010, 010.3640, 280.1910.

1. Introduction

Atmospheric chemistry is dominated by cycles of ozone and water vapor. It is known that photochemical formation is one important source of tropospheric ozone.[1] In the southern tropics, ozone precursors result mostly from episodic events such as biomass burning and are causing a significant increase in tropospheric ozone.[2] Moreover, recent numerical studies have pointed out the role of acetone and peroxides in ozone production in the upper tropical troposphere.[3] However, the stratosphere and the troposphere are dynamically coupled, and the global climate is highly dependent on ozone changes in the upper troposphere and on exchanges between the stratosphere and the troposphere. This makes the upper troposphere a key zone, especially in the tropics, where many complex and interconnected chemical and dynamic mechanisms occur. From a dynamic point of view, stratospheric inputs into the troposphere linked to the subtropical jet stream could be important.[4–6] The role of deep tropical convection has been studied with MOZAIC (Measurement of OZone and water vapor by Airbus In service airCraft[7]) data and with radiosounding and model data.[8] For many years, observing and understanding the physical and chemical states of the stratosphere have been important objectives of the scientific community. Since 1993, in the framework of the network of detection of stratospheric changes,[9] Rayleigh–Mie lidar measurements of stratospheric aerosols and temperature have been carried out in the southern tropics at the University of Reunion.[10]

Yet, despite this scientific interest in both tropical stratosphere and troposphere, there is a significant lack of tropospheric ozone measurements in the tropical and equatorial regions. Ozonosonde stations are confined mostly to the midlatitude Northern Hemisphere.[11,12] The development of ground-based lidar stations whose research would include making ozone measurements could improve this situation. The technique of tropospheric ozone lidar measure-

J.-L. Baray, J. Leveau, F. Posny, and S. Baldy are with the Laboratoire de Physique de l'Atmosphere, Reunion University, 15 avenue R. Cassin, 97715 St. Denis Cedex, Reunion Island, France. The e-mail address for J.-L. Baray is barray@univ-reunion.fr. J. Porteneuve, G. Ancellet, and P. Keckhut are with Service d'Aeronomie, B. P. 3 91371 Verriere-le-Buisson Cedex, France.

Received 1 March 1999; revised manuscript received 2 August 1999.

0003-6935/99/336808-10$15.00/0

ments by differential absorption between two wavelengths has been known for a long time and is well developed.[13] Many lidar stations throughout the world operate in a routine mode, mainly in the midlatitudes.[14–22] A ground-based lidar station is well suited for monitoring the troposphere with good continuity of measurement and for studying short-time-scale events such as tropopause folds and stratosphere–troposphere exchange induced by the tropical convective activity, i.e., for long-term climatological survey and flux studies. To meet these scientific objectives, it should be quite valuable to develop a differential absorption lidar to measure the troposphe at Reunion Island. Most tropospheric ozone lidars are currently operating within the framework of urban pollution studies and are located at midlatitudes where the tropopause is rather low. The range of the existing tropospheric ozone lidar thus does not exceed 12–13 km. For example, an installation such as the Observatoire de Haute Provence station, with only one mirror of reception, would probably not be sufficient for use in achieving our measurement goal, that of the tropical high troposphere, which is higher than at average latitudes (16–17 km). At Reunion University, a lidar devoted to atmospheric monitoring already exists. This Rayleigh lidar measures aerosols and temperature in the stratosphere and the mesosphere, using a mosaic of four telescopes with a total area of 0.78 m^2.[10] It would be interesting to imagine a system that would allow the same reception component to be used for two modes, stratospheric Rayleigh and tropospheric ozone. Moreover, having a single instrument for several measurements would provide a great opportunity to reduce the human and financial resources needed for its operation. However, stratospheric and tropospheric lidars have different requirements for laser power and wavelength, field of view, noise, etc. In this paper we present an integration solution, developed and tested at Reunion Island, for tropospheric ozone lidar implementation with a Rayleigh–Mie system. The setup of the Rayleigh–Mie lidar at Reunion Station is described in Section 2. Integration and technical choice justifications, performance evaluation, experimental arrangement, data processing, and error analysis are described in Section 3. First results and comparisons with electrochemical cell (ECC) soundings are presented and discussed in Section 4.

2. Lidar Chronological Setup at the Reunion Station

A schematic of the optical part of the Rayleigh–Mie lidar at Reunion Station is shown in Fig. 1. This station was installed in 1993 to monitor stratospheric and mesospheric aerosols in the southern tropics.[10] The first laser emission was made by the second harmonic of a Nd:YAG pulsed laser at 532 nm with a 10-Hz repetition rate and an energy of 300 mJ per pulse. In this first version, the optical receiving system was a parabolic telescope (diameter, 530 mm). After prospecting and validation, routine measurements began in 1994. Evolution of the system has

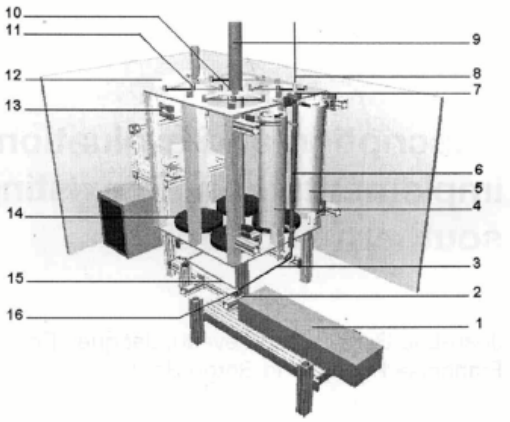

Fig. 1. Schematic representation of the Reunion lidar system: 1, laser; 2, KDP crystals; 3, 266-nm beam; 4, polarized channel telescope; 5, B channel telescope; 6, Raman cell; 7, divergence optimizer; 8, 289–316-nm beam; 9, 532–1064-nm beam; 10, Rayleigh afocal dioptric; 11, location of optical fiber fixation; 12, spectrometer; 13, PMT's; 14, B channel telescope; 15, 532–1064-nm beam; 16, 266-nm removable mirror. For ozone measurements the removable mirror (16) deflects the 266-nm beam, which is then deflected upward in the Raman cell. For Rayleigh measurements, mirror 16 is turned off and the 532–1064-nm beam is deflected upward at the middle of the four parabolic mirrors (14).

improved the system's performance. The reception system was upgraded to four receiving telescopes (diameter, 500 mm; point 14 in Fig. 1). In November 1995 this system was further upgraded by installation of a second optical channel of lower sensitivity with a smaller-diameter telescope (200 mm; point 4 in Fig. 1). The use of smaller telescopes allows the signal intensity to be reduced and the range of altitude probed during routine measurements to be extended downward. This solution was preferred to the use of a dichroic mirror as at other French stations.[23] In March 1996 the laser source was replaced by a new Nd:YAG laser emitting with a power of 500 mJ per pulse and a 30-Hz repetition rate (point 1 in Fig. 1). In November 1996 the installation of dioptric afocal optics (point 10 in Fig. 1) that comprises one concave lens (diameter, 25 mm) and one output double lens (diameter, 160 mm) allowed the 532- and 1064-nm beam divergence to be reduced by a factor of 12. Polarized channels have also been added (point 5 in Fig. 1). In November 1997 six simultaneous counting channels began operating, including the infrared fundamental Nd:YAG emission. The combination of these wavelength emissions and polarized channels permits a better characterization of aerosols in the upper troposphere and stratosphere.[24] The station has now been running in routine mode for four years. The numbers of nighttime measurements made during this period are listed in Table 1. Finally, in June 1998 the tropospheric ozone extension was installed.

Table 1. Nighttime Measurements of the Reunion Lidar Station from 1994 to 1999

Year	Number of Nights
1994	74
1995	93
1996	150
1997	127
1998	120[a]
1999	65[b]

[a]With 31 O_3 measurements
[b]Until April, with 16 O_3 measurements.

3. Description of the Tropospheric Ozone Measurement System

The ozone measurement technique is based on the principle of differential absorption by ozone of an ultraviolet beam.[25] Electronic and computing processing permit retrieval of the ozone profile. Considering the technical constraints that are linked to the actual Rayleigh lidar, use of the Nd:YAG laser of the NDSC (Network for the Detection of Stratospheric Change) Station was imperative. Many useful wavelengths for tropospheric ozone measurements can be generated by stimulated Raman scattering of the fourth harmonic of the Nd:YAG laser in hydrogen and deuterium (Table 2). Inasmuch as our scientific objectives include upper-tropospheric measurements, the lidar range should reach the tropopause, which is quite high in the tropics (near 17 km). As indicated in Table 2, the 266-nm wavelength is obtained directly with the fourth harmonic of the Nd:YAG laser and is generally used as the absorbed wavelength for the lowest kilometers of the atmosphere (the boundary layer). It is not possible to use it for the upper troposphere because this wavelength is absorbed too much by ozone. Molina and Molina[28] have determined the ozone absorption coefficient for a mixing ratio near the ground of 38 parts in 10^9 by volume (ppbv): 947×10^{-3} km^{-1} for a 266-nm beam, 159×10^{-3} km^{-1} for a 289-nm beam, and 4.6×10^{-3} km^{-1} for a 316-nm beam. Wavelengths longer than 340 nm are not absorbed sufficiently to have sufficient sensitivity in the troposphere and are useful only for stratospheric measurements. Some previous studies[15,26] showed that the choice of an excimer laser was not necessarily optimum for tropospheric ozone measurements. Hence, considering on one hand the technical and financial constraints and on the other hand our scientific objective to reach near the tropical tropopause, the most feasible choice, and the one that was made, was to consider the wavelength coupling (289–316 nm) obtained by stimulated Raman scattering shifting in a single deuterium Raman cell. Moreover, using a unique cell to provide both wavelengths is a great advantage for reducing any differential misalignment between emission and collectors. It is useful to evaluate the performance of the theoretical signal by using the optical coefficients and quantum efficiencies of the existing system to gain a theoretical appreciation of the utility of this system for ozone measurement.

Table 2. Available Wavelengths with a Nd:YAG Laser and Typical Efficiencies of Stimulated Raman Scattering in Hydrogen and Deuterium

Wavelength (nm)	Type of Stimulated Raman Scattering	Maximal efficiency (%) Papayannis[a]	Ancellet and Ravetta[b]
266	None (×4)	–	–
289	$S1$, D_2	30	38
299	$S1$, H_2	30	36
316	$S2$, D_2	15	18
341	$S2$, H_2	20	35
349	$S3$, D_2	4	–
355	None (×3)	–	–
397	$S3$, H_2	4	–

[a]Ref. 26.
[b]Ref. 27.

A. Performance Evaluation

For a single pulse, the strength of return signal S depends on the distance r from the telescope to the scattering event and on the wavelength λ. This dependence is given by the formula

$$S(r, \lambda) = \frac{A(\lambda)}{r^2} \beta(r, \lambda) \exp\left[-2 \int_0^r \alpha(r', \lambda) dr'\right], \quad (1)$$

where $A(\lambda)$ is a system constant that includes the level of laser pulse energy, the telescope area, the optical detector efficiency, and the photomultiplier tube (PMT) quantum efficiency; β is the atmospheric volume backscatter radiation (Rayleigh and Mie); and α is the atmospheric volume extinction coefficient (Rayleigh, Mie, and ozone). Because Reunion Station is located at sea level in a tropical oceanic environment, strong humidity and marine aerosols are expected in the marine boundary layer. Hence the optical thickness for the lowest layer is set to 1.6.[29,30] By using optical and electronic constants of the lidar system and by imposing ozone and density profiles obtained from radiosounding climatology at the Reunion site,[8] we can evaluate the strength of the return signal as a function of wavelength (Fig. 2). Our simulations permit only an evaluation of the magnitude order, because it is difficult to take account the following operating conditions:

(1) We consider that the fields of view of the receiver completely overlap that of the transmitter.
(2) We neglect the effects of multiple scattering events.
(3) We assume that the counting system works in a perfectly linear way (which is not the case for upper-tropospheric measurements). The linearity of the counting is limited by the bandpass of the system. The comparison of two similar systems that are receiving a backscattered signal from the same portion

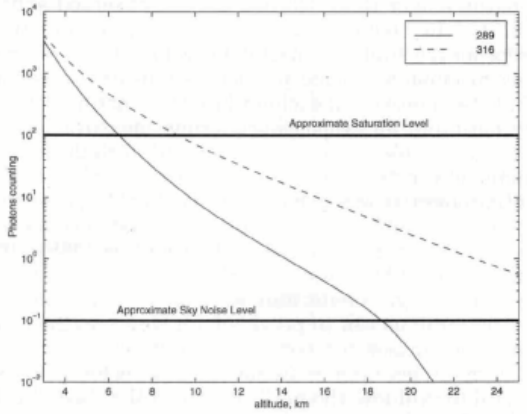

Fig. 2. Modeled wintertime backscatter return photon counting, for the 289–316-nm wavelength couple, compared with typical counting saturation and sky noise levels.

of the sky with one attenuated because it uses a glass splitter allows us to verify that our system is linear (uncertainty, <0.1%) as soon as less than one photon per shot per microsecond arrives on the photocathode.

Despite the use of the approximations mentioned above, these simulations are useful in evaluation of the potentiality of the lidar system and of the wavelength coupling within a tropical context (strong humidity in the lowest layers; tropopause level, 17 km). As was seen by Proffitt and Langford,[21] the return signal increases with wavelength and decreases by a factor of 10^4 between the lowest layers and the upper troposphere. The results of this simulation emphasize two points:

(1) The lowest sounded layers are likely saturated by the photon-counting system. Hence the use of an analog processing mode, alone or in combination with the photocounting mode, should be necessary for processing the signal from the lower troposphere.

(2) The upper-range limit of the system is close to the altitude of the tropical tropopause. Below 18 km, the simulated signal is significantly superior to the typical night sky noise level observed at these wavelengths by a typical ground-based lidar station (Fig. 2).

B. Technical Description of the Emission System

The fourth-harmonic Nd:YAG (266 nm) is obtained by the nonlinear effects of two successive passages in potassium dihydrogen phosphate (KDP) crystals located at the output of the laser. The two emitted wavelengths, 289 nm (absorbed by ozone, ON channel) and 316 nm (nonabsorbed, OFF channel), are generated by stimulated Raman scattering in a deuterium high-pressure cell in which the 266-nm beam is focused by a lens that comprises silica windows. The characteristics of the emission system are listed in Table 3. These two wavelengths correspond to the first and second Stokes lines for deuterium. The energy-conversion efficiency depends mainly on the active gas pressure in the Raman cell,[31] on the focal distance of the window lenses, and on the quality and the power of the beam that is entering the cell.[32] In the present system the 266-nm beam is deflected 90° by two UV mirrors, one of which is removable to permit switching between two operating modes. It then enters the Raman cell, which is placed in a vertical position (point 6 in Fig. 1). The Raman cell is equipped with two silica window lenses that have diameters adapted to the beam and a focal distance of 75 cm to focus the beam as closely as possible to the center of the cell for optimal stimulated Raman scattering. Generation of an UV beam by the Raman diffusion principle is not without consequences for the quality of the emitted beam. Indeed, disruptions by nonlinear phenomena and chromatic aberrations take place in the high-pressure Raman cell and degrade the quality of the emitted beam. To minimize the deleterious consequences of this effect, we place an optical system at the output of the Raman cell to reduce the emitted beam divergence to 0.25 mrad (Table 3). This value corresponds to one quarter of the field of view of the telescope. This system comprises three lenses, whose disposition and composition are shown in Fig. 3.

Table 3. Emission Characteristics

Subsystem	Parameter	Value
Laser	Energy at 255 nm	40 mJ/pulse
	Frequency	30 Hz
	Beam diameter	10 mm
	Divergence of 266-nm beam	0.70 mrad
Raman cell	Length	1500 mm
	Diameter (in/out)	20/55 mm
	D_2 pressure/purity	10 bars/99.7%
	He pressure/purity	24 bars/99.999%
Optical system to reduce divergence	Beam expander for 289–316-nm magnification	3.2
	Output diameter of beams	30 mm
	Divergence of emitted beam	0.25 mrad

C. Technical Description of the Reception System

For measurements of stratospheric temperature and aerosols the 532-nm backscattered beam is collected by an optical fiber system. One 0.4-mm fiber is located at the focal point of each telescope and is used to transport the collected signal to the electronic detection units. This collection method allows the collecting area to be increased without the need for using a unique, costly mirror. In the integration of the new ozone lidar system, the same telescopes as for the stratospheric measurements at 532 nm are

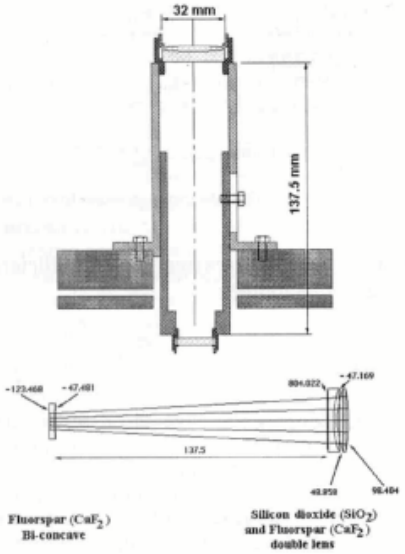

Fig. 3. Optical system used to minimize the divergence of the UV emitted beams (289 and 316 nm).

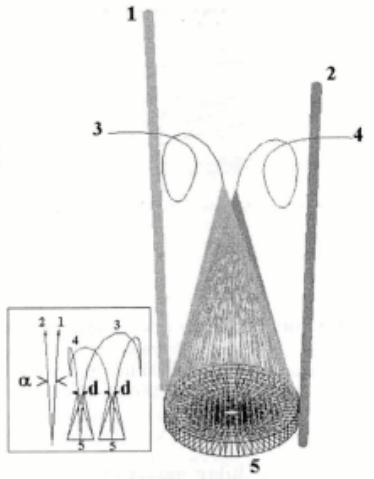

Fig. 4. MFC system: 1, UV emitted beam; 2, visible emitted beam (for stratospheric temperature and aerosol measurements); 3, UV fiber; 4, visible fiber; 5, receiving telescopes. For each telescope the linear distance d = 3.3 mm between the two fibers corresponds to the angular distance α between the two beams.

used. For stratospheric temperature and aerosol measurements the choice of a small field of view permits a compromise between the noise level and the vertical range; hence the use of 0.4-mm fibers. However, because of differences in beam emission divergences and in expected vertical measurement ranges, the use of these existing optical fibers is not possible for the differential absorbing lidar configuration. The ozone channels require a larger field of view for the telescopes to obtain full beam recovery in the expected altitude range (mid and upper tropical troposphere); hence larger-diameter optical fibers (1.5 mm) are required. Their diameter is inferred from the calculation of the spot size in the focal plane where the optical fiber is implemented and results from a larger beam divergence and from the defocusing effect for short vertical ranges. (The image of a scattering volume not strictly located at infinity is not found exactly at the focus of the receiver.[33]) Above 2 km, the 1.5-mm fiber diameter is closer to the defocalization distance, as indicated in Table 4. This configuration provides the full collection of backscattered UV signals in the required vertical range. To permit both measurements (stratospheric temperature and aerosols, and tropospheric ozone) to be made with the same collecting set, a mechanical system that holds a couple of fibers was thus developed: the multiple fiber collector (MFC; Fig. 4 and point 11 in Fig. 1). For each telescope, the linear distance d between the two fibers corresponds to the angular distance α between the UV (for tropospheric ozone measurements) and the visible (for stratospheric temperature and aerosols) beams (Fig. 5 and point 12 in Fig. 1). Both fiber positions can be adjusted at the focal point to keep the fields of view of the telescopes in phase. The advantage of using the MFC is the possibility of being able to use the same optical col-

Table 4. Calculation as a Function of Height *Z* of Defocalization Distance *Df*, Parallax *P*, Spot Size *Tz*, and Spot Size in the Focal Plane *Tf* for the Optical Fiber Dedicated for Ozone Measurements and of Geometrical Factor *Fg* for the Optical Fiber Dedicated for Rayleigh Measurements[a]

Z (km)	*Df* (mm)	*P* (mm)	*Tz* (mm)	*Tf* (mm)	*Fg* (%)
2	1.13	0.75	0.821	1.383	34.3
4	0.56	0.38	0.623	0.904	61.1
6	0.38	0.25	0.557	0.744	77.4
8	0.28	0.19	0.524	0.664	87.3
10	0.23	0.15	0.504	0.617	93.4
12	0.19	0.13	0.491	0.585	97.1
14	0.16	0.11	0.481	0.562	99.3
16	0.14	0.09	0.474	0.545	100
18	0.13	0.08	0.469	0.531	100

[a]The geometrical factor for the optical fiber dedicated for ozone measurements is 100% over 2 km, and the ozone system permits a large latitude for alignment.

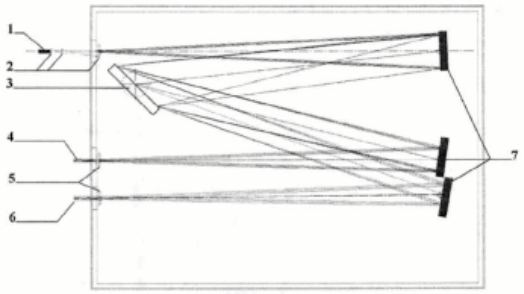

Fig. 5. Spectrometer formed by a holographic grating and two spherical mirrors: 1, four-fiber terminal transmitting the 289–316-nm beam; 2, adaptive lens; 3, 3600-line/mm grating; 4,289-nm PMT; 5, adaptive lens; 6, 316-nm PMT; 7, spherical mirror.

lectors for different lidar measurements. The optical system allows an image quality (pulse response of a star image located at infinity) associated with the atmospheric turbulence of 0.8 mrad to be obtained. With reference to the part associated with the quality of the receiving telescopes, 90% of the energy is included in 0.6 mrad.

Spectral separation of 289- and 316-nm beams is obtained with a spectrometer that includes a Czerny–Turner holographic grating (Fig. 4). After a system of three lenses used to reduce the divergence of the beam by a factor of 3 and to adapt the numerical aperture of the fibers to that of the grating, the backscattered beam is separated by a high-performance grating (3600 lines/mm). Then each beam is redirected toward PMT's by concave mirrors. The noncooled bialkali Hamamatsu R1527P PMT's used for the ozone channels are preamplified. These PMT's provide good sensitivity in the near-UV spectral range. Typical voltage operation is less than 900 V to limit the signal-induced bias associated with the PMT response to an intense luminous pulse.[34] The electronic system includes analog channels (of 15-m resolution) for the lower layers and photon-counting channels (of 150-m resolution) for the high layers, for each wavelength 289 and 316 nm. The signal-processing electronic chain is rather similar to those used for the OHP ozone lidar station at the Observatoire de Haute Provence[15] and for the Airborne Lidar for Tropospheric Ozone (ALTO).[27]

D. Data Processing: Signal Inversion and Error Analysis

The ozone concentration (in molecules per cubic meter) is deduced from the lidar backscattered signal by use of the following equation:

$$c_{O_3} = \frac{1}{2\Delta\sigma}\frac{\mathrm{d}}{\mathrm{d}r}\ln\left(\frac{p^{\mathrm{off}}}{p^{\mathrm{on}}}\right). \quad (2)$$

To take account of the Rayleigh scattering by the atmospheric molecules, using the Rayleigh molecular extinction (α) and backscattering (β) coefficients, we modify Eq. (2) as follows[35]:

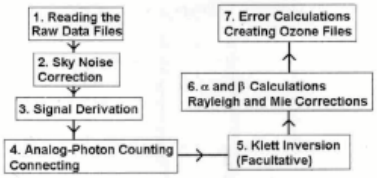

Fig. 6. Algorithm to calculate ozone profiles from raw data.

$$c_{O_3} = \frac{1}{2\Delta\sigma}\frac{\mathrm{d}}{\mathrm{d}r}\ln\left(\frac{p^{\mathrm{off}}}{p^{\mathrm{on}}}\right) - \frac{1}{2\Delta\sigma}\frac{\mathrm{d}}{\mathrm{d}r}\ln\left(\frac{\beta^{\mathrm{off}}}{\beta^{\mathrm{on}}}\right) - \frac{\Delta\alpha}{\Delta\sigma}. \quad (3)$$

Data processing is then based on differential absorption of two wavelengths by ozone and on the assumption that the two wavelengths are close enough that the backscattering coefficients are practically identical for the two beams. [The dependence law is $\alpha = \alpha_0(\lambda)^{-k}$, with k varying from 0, in the presence of cirrus clouds, to 2. For typical values at the wavelengths 289 and 316 nm, the differential extinction that is due to aerosol background is smaller by 1 or 2 orders of magnitude than the Rayleigh extinction, as measurements are performed only for cloud-free conditions or with cirrus.] The calculation of ozone concentration is based on Eq. (3) with the algorithm described in Fig. 6. After it reads the raw data, the lidar signal is normalized and corrected for the inverse square range dependence. The signal is corrected for the sky noise component by polynomial or exponential interpolation, separately on each channel, between two levels at the end of the signal. The correction for possible radio-frequency interference of the laser can also be applied in our algorithm by generation of a noise file obtained by blocking the laser. The range-corrected signal is smoothed after numerical low-pass digital filtering, which corresponds to a second-order polynomial fit over a number of points that increases with altitude. We then obtain the terms p^{off} and p^{on} of Eq. (3). The analog and photon-counting slope signals are then combined by use of an analog signal in the low layer and a photon-counting signal in the upper layer. The connection between the two is made by linear mixing in a layer whose height and thickness are chosen as functions of the lidar signal (generally 1 km, near 6-km height). The correction for the influence of strong aerosol layers by the method of Klett[36,37] can be applied in our processing algorithm if necessary. However, this correction does not significantly improve the ozone profiles in the free troposphere and is not used for our lidar system. The aerosol backscatter coefficient is calculated at 316 nm, where ozone absorption is negligible, by a backward integration scheme in which the Rayleigh backscatter is taken into account.[38,39] If the aerosol layer is significant (cloud), data are removed from the profile at the cloud altitude. The numerical filter applied to calculate

the signal derivative is also used to differentiate the aerosol backscatter profiles. In the Eq. (3), coefficients α and β depend on the atmospheric density profile calculated by means of an atmospheric standard-atmosphere model whose main characteristics (vertical temperature gradient, ground temperature, tropopause height) are adjustable. Knowing the difference of absorption $\Delta\sigma$ between ON and OFF channels calculated by Bass and Paur,[40] we are able to have access to the vertical ozone concentration.

Lidar ozone measurement is subject to errors, which are either systematic or statistical. Systematic errors originate from the contribution on the signal of chemical species other than ozone. The influence of nitrogen dioxide (NO_2) absorption[41] and sulfur dioxide (SO_2) absorption[42] was evaluated. At a 38-ppbv mixing ratio, the absorption coefficients at 289 and 316 nm, respectively, are 9×10^{-3} and 7×10^{-3} km^{-1} for SO_2 and 8.6×10^{-3} and 24×10^{-3} km^{-1} for NO_2. The influences of SO_2 and NO_2 are then relevant only in the boundary layer, where the concentration of these pollutants can be potentially high, and are negligible in the free troposphere.[27]

Another type of error comprises statistical errors associated with the signal and sky noise fluctuations. For the analog mode one calculates the statistical error from the root mean square of the signal in the noise region. For the photon-counting mode one calculates the error by assuming that the signal's standard deviation is equal to that which is expected for a Poisson statistical distribution of detected photons. The error is thus estimated directly from the signal intensity. Donovan *et al.* found that a pure Poisson statistic overestimates the error compared with that which they derive in their method in which error depends on sampling time, width of pulse, and observed count rate.[43] However, when the PMT is saturated, the counting is no longer Poissonian. Even when the counting is not saturated, it is slightly different from Poissonian counting according to the position of the discriminator that separates the noise pulse from the signal pulse. The discriminator disturbs the statistic: if it is too low, it counts the noise pulse; if it is too high it does not count all the signal pulse and the count is less than expected.[44] The discriminator is adjusted to provide the best compromise, and the counting distribution does not vary more than 10% from theory. Other recent studies showed that the Poissonian method underestimates the statistical signal and then cannot be applied successfully for an analog signal in the lower troposphere.[45] However, Poisson's law remains a good estimation of the statistical error, especially for an upper-tropospheric photon-counting signal. In Section 4, error bars attached to ozone profiles are evaluated from these considerations.

4. Results and Comparisons

In this section we present results obtained in austral winter 1998 from the Reunion ozone lidar. One of the first ozone measurement obtained by lidar at Reunion Island was made on 26 June 1998. Slopes of the channels are shown in Fig. 7. For that profile, 289- and 316-nm photocounting channels are saturated below 5 and 6 km, respectively, and reach 16 km. Hence the use of analog channels makes available ozone measurements between 3 and 7 km. Below 3 km the recovery between reception and emission fields is not sufficient to provide useful data. Above 10 km (289-nm signal) and 14 km (316-nm signal) the analog signal is too weak and there is too much sky noise relative to the signal. Thus the connection between analog and photocounting channels is made between 7 and 8 km (Fig. 7). The corresponding ozone profile is presented in Fig. 8. For the

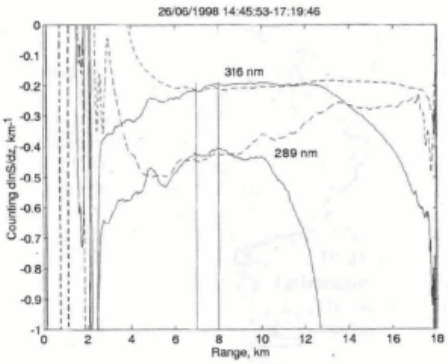

Fig. 7. Range derivative of the logarithm of the range-corrected lidar signal corresponding to photocounting (dashed curves) and analog (solid curves) detection of the two wavelengths 289 and 316 nm on 26 June 1998. We computed the range-corrected profiles by exponentially correcting the sky noise signal over 21 km for the 289-nm channel and over 31 km for the 316-nm channel. The connection between analog and photocounting channels was made between 7 and 8 km. In this and the following figures the data on which the measurements were made are given in day–month–year order, followed by the local time (hours–minutes-seconds) during which the measurements were made.

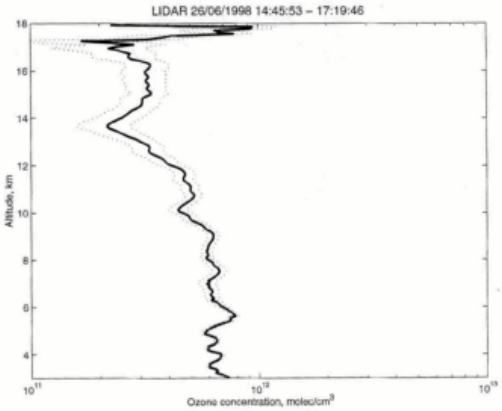

Fig. 8. Corresponding ozone profile (see Fig. 7) for 26 June 1998.

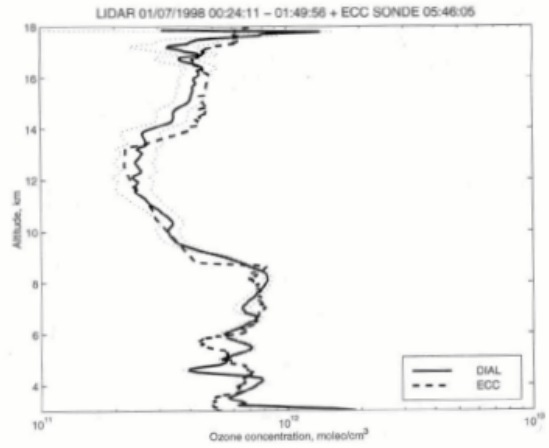

Fig. 9. Ozone concentrations obtained by lidar on 1 July 1998 (acquisition time, 1 h and 25 min) compared with the profile obtained by an ECC sonde 5 h later. Solid curve, lidar profiles; dotted curves, statistical error intervals for lidar measurements; dashed curves, ECC profiles.

measurements on 26 June the upper-range limit is ~14 km. Results from 14 to 18 km are uncertain because the signal is weak and noisy. The upper limit depends on clear sky conditions, on alignment of the reception system, and on measurement integration time and reaches the tropical tropopause (17 km) for clear sky conditions.

After the first profiles were obtained during June 1998, the lidar operated almost daily during July 1998, in the framework of the European campaign TRACAS (TRAnsport of Chemical species Across the Subtropical tropopause). Two measurement comparisons between lidar and radiosounding were made, on 1 July (Fig. 9) and on 29 July (Fig. 10).

Fig. 10. Ozone concentrations obtained by lidar on 29 July 1998 (acquisition time, 2 h and 20 min) compared with the profile obtained nearly simultaneously by electrochemical sonde.

Ozone radiosounding profiles are obtained with the ECC standard processing calculator, used with a T_{max} interface and coupled with a Vaisala RS80 radiosonde.[2] The relative precision of ECC ozone measurements in the troposphere was found to be by field tests 10%.[46] Comparisons with ECC sounding (Figs. 9 and 10) globally show good agreement between the two techniques. After ozone concentration was converted to mixing ratio by use of temperature and pressure profiles obtained with radiosondes, the average difference between the two profiles was calculated from 4 to 14 km and is less than 7.5 ppbv for the 1 July profile and less than 6.5 ppbv for the 29 July profile. These values have less than the precision of the two measurement techniques. However, one can note some difference between the ECC sonde and lidar profiles, mainly in the lower layers on 1 July (Fig. 9) and in the upper troposphere on 29 July (Fig. 10). For the first comparison (Fig. 9) the measurements were not obtained simultaneously (nearly a 5-h interval). For the second comparison (Fig. 10), even when measurements were obtained simultaneously, a simple advection calculation that used horizontal wind data obtained with the European global model data [ECMWF (European Center for Medium Range Weather Forecast)] and the vertical advection measured by the radiosonde indicates a displacement of the balloon of more than 65 km between the launch and the tropopause level measure. Hence, ECMWF data indicate the presence of the subtropical jet stream over Reunion Island on 1 July and 29 July, with wind speed greater than 30 m s^{-1} over 300 hPa. The lidar provides vertical measurements and then not exactly the same measurements as an ECC sonde, which are advected by the wind.

We further note that this lidar system can follow the tropospheric ozone evolution on short time scales. For example, Fig. 11 shows the evolution, in increments of 20 min, of the tropospheric ozone mixing ratio profile observed on 29 July. One can indeed notice the interesting ozone maximum observed by lidar from 6 to 8 km, which is associated with tropopause folding under the subtropical jet stream. The time of integration used to build each elementary profile is sufficient to trace ozone short-time variability up to 13–14 km. Above that level the analysis of ozone values must be done with great care because the measurement uncertainty becomes significant. Figure 11 shows that the tropospheric ozone above Reunion Island has a short-term variability (in time and space) that is consistent with differences between ECC sonde and lidar observed on comparison (Figs. 9 and 10). The results presented in this section clearly illustrate the capability of this instrument to provide experimental data for the study of stratosphere–troposphere mass exchanges in the tropics.

5. Concluding Remarks

Our scientific objectives are to measure ozone in the high tropical troposphere. To limit the cost and maintenance of the lidar system we integrated it with

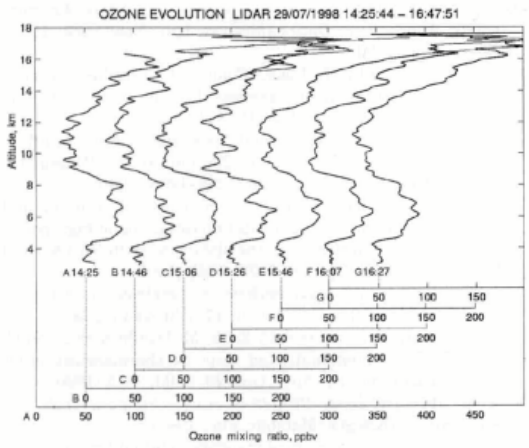

Fig. 11. Ozone mixing ratio evolution during the time from 14:25:44 (profile A) to 16:47:51 (profile G) universal time as observed by lidar at Reunion on 29 July 1998. The temporal file summation is 20 min (36,000 shots). The profiles have been offset successively by 50 ppbv.

an existing Rayleigh–Mie lidar system. Using the same laser source as the Rayleigh–Mie system, the unique Raman cell reduces problems of misalignment, and the emission afocally reduces the field of view and noise. For the reception, the use of optical fibers permits thermal and mechanical separation of the reception part and the analysis part of the system. The MFC system allows sharing of collecting surfaces for different fields of view. The spectrometer was studied for optimum spectral separation in the UV. The electronic system (PMT and analog mode) allows a large altitude range to be covered.

When the requisite conditions are achieved (clear sky and optimal alignment of the reception system), the lidar system permits ozone measurement from 3 to 17 km, the altitude of the tropical tropopause. Comparisons with ECC ozone soundings show good agreement between the two techniques. The average difference in the troposphere observed on several joined soundings does not exceed 8 ppbv. We have also shown the capability of the lidar to study tropospheric ozone evolution in tropics. The significant lack of tropospheric ozone measurements in the tropical and equatorial regions makes this lidar implementation useful and technically conceivable for many Rayleigh–Mie lidar stations. At a site such as Reunion Island, where we wish to conduct various studies (stratosphere–troposphere exchange linked to the subtropical jet stream, study of tropical convection and influence of biomass burning), scientific interest in this extension of the Reunion lidar system is substantial. It will permit an increase in the database of ozone profiles that have been obtained by semimonthly radiosoundings launched from Reunion since 1992 (Ref. 2) and in particular offers the possibility of studying ozone evolution on a shorter temporal scale than those permitted by radiosounding.

The Reunion lidar development has been supported by the French Centre National de la Recherche Scientifique/Institut National des Sciences de l'Univers and Conseil Régional de la Réunion. The July 1998 TRACAS campaign (radiosondes and lidar data) was supported by European Community grant ENV4-CT97-0520. We gratefully acknowledge the assistance of the Service d'Aéronomie technical staff (J. L. Conrad, F. Fassina, C. Laqui, J. P. Marcovici, A. Théodon, and P. Weill) and the Laboratoire de Physique de l'Atmosphère radiosounding team (G. Bain, D. Faduilhe, J. M. Metzger, T. Portafaix, and S. Roumeau).

References

1. World Meteorological Organization, "Scientific assessment on ozone depletion," Tech. Rep. 37, Global Ozone Research Monitoring Project (World Health Organization, Geneva, 1994).
2. S. Baldy, G. Ancellet, M. Bessafi, A. Badr, and D. Lan Sun Luk, "Field observation of the vertical distribution of tropospheric ozone at the island of Reunion (southern tropics)," J. Geophys. Res. **96,** 23,835–23,849 (1996).
3. I. Folkins, R. Chatfield, H. Singh, Y. Chen, and B. Heikes, "Ozone production efficiencies of acetone and peroxides in the upper troposphere," Geophys. Res. Lett. **25,** 1305–1308 (1998).
4. H. Gouget, J. P. Cammas, A. Marenco, R. Rosset, and I. Jonquières, "Ozone peaks associated with a subtropical tropopause fold and with the trade wind inversion: a case study from the airborne campaign TROPOZ II over the Caribbean in winter," J. Geophys. Res. **101,** 25,979–25,993 (1996).
5. J. L. Baray, G. Ancellet, F. G. Taupin, M. Bessafi, S. Baldy, and P. Keckhut, "Subtropical tropopause break as a possible stratospheric source of ozone in the tropical troposphere," J. Atmos. Terr. Phys. **60,** 27–36 (1998).
6. J. P. Cammas, S. Jacobi-Koaly, K. Suhre, R. Rosset, and A. Marenco, "Atlantic subtropical potential vorticity barrier as seen by Measurements of Ozone by Airbus In Service Aircraft (MOZAIC) flights," J. Geophys. Res. **103,** 25,681–25,693 (1998).
7. K. Suhre, J. P. Cammas, P. Nédelec, R. Rosset, A. Marenco, and H. G. J. Smit, "Ozone-rich transients in the upper equatorial Atlantic troposphere," Nature **388,** 661–663 (1997).
8. J. L. Baray, G. Ancellet, T. Randriambelo, and S. Baldy, "Tropical Marlene cyclone and stratosphere–troposphere exchange," J. Geophys. Res. **104,** 13,953–13,970 (1999).
9. M. J. Kurylo and S. Solomon, "Network for the detection of stratospheric change: a status and implementation report," NASA and NOAA Special Rep. (NASA, Washington, D.C., 1990).
10. H. Bencherif, J. Leveau, J. Porteneuve, P. Keckhut, A. Hauchecorne, G. Mégie, F. Fassina, and M. Bessafi, "Lidar development and observations over Reunion Island (20.8 °S, 55.5 °E)," in *Proceedings of the 18th International Laser Radar Conference*, A. Ansmann, R. Neuber, P. Rairoux, and U. Wandinger (Springer-Verlag, Berlin, 1996), pp. 553–556.
11. J. A. Logan, "Trends in the vertical distribution of ozone: an analysis of ozonesonde data," J. Geophys. Res. **99,** 25,535–25,585 (1994).
12. G. Ancellet and M. Beekmann, "Evidence for changes in the ozone concentrations in the free troposphere over southern France from 1976 to 1995," Atmos. Environ. **31,** 2835–2851 (1997).
13. J. Pelon and G. Mégie, "Ozone monitoring in the troposphere and lower stratosphere: evaluation and operation of a

ground-based lidar station," J. Geophys. Res. **87,** 4947–4955 (1982).
14. O. Uchino, M. Tokunaga, M. Maeda, and Y. Miyazoe, "Differential absorption lidar measurements of tropospheric ozone with an excimer–Raman hybrid laser," Opt. Lett. **8,** 347–349 (1983).
15. G. Ancellet, A. Papayannis, J. Pelon, and G. Mégie, "DIAL tropospheric measurement, using a Nd:YAG laser and the Raman shifting technique," J. Atmos. Ocean. Technol. **6,** 832–839 (1989).
16. L. Stefanutti, F. Castagnoli, M. Del Guasta, M. Morandi, V. M. Sacco, L. Zuccagnoli, S. Godin, G. Mégie, and J. Porteneuve, "The Antarctic ozone LIDAR system," Appl. Phys. B **55,** 3–12 (1992).
17. U. Kempfer, W. Carnuth, R. Lotz, and T. Trickl, "A wide-range ultraviolet lidar system for tropospheric ozone measurements: development and application," Rev. Sci. Instrum. **65,** 3145–3164 (1994).
18. J. A. Sunesson, A. Apituley, and D. P. J. Swart, "Differential absorption lidar system for routine monitoring of tropospheric ozone," Appl. Opt. **33,** 7045–7058 (1994).
19. J. Reichardt, U. Wandinger, M. Serwazi, and C. Weitkamp, "Combined Raman lidar for aerosol, ozone, and moisture measurements," Opt. Eng. **35,** 1457–1465 (1996).
20. Z. Wang, J. Zhou, H. Hu, and Z. Gong, "Evaluation of dual differential absorption lidar based on Raman-shifted Nd:YAG or KrF laser for tropospheric ozone measurements," Appl. Phys. B. **62,** 143–147 (1996).
21. M. H. Proffitt and A. O. Langford, "Ground-based differential absorption lidar system for day or night measurements of ozone throughout the free troposphere," Appl. Opt. **36,** 2568–2585 (1997).
22. L. Fiorani, B. Calpini, L. Jaquet, H. Van Den Bergh, and E. Durieux, "A combined determination of wind velocities and ozone concentrations for a first measurement of ozone fluxes with a DIAL instrument during the medcaphot-trace campaign," Atmos. Environ. **32,** 2151–2159 (1998).
23. P. Keckhut, A. Hauchecorne, and M. L. Chanin, "A critical review of the database acquired for the long term surveillance of the middle atmosphere by the French Rayleigh lidar," J. Atmos. Ocean. Technol. **10,** 850–867 (1993).
24. K. Sassen, "Advances in polarization diversity lidar for cloud remote sensing," Proc. IEEE **82,** 1907–1914 (1994).
25. G. Mégie and R. T. Menzies, "Complementarity of UV and IR differential absorption lidar for global measurements of atmospheric species," Appl. Opt. **19,** 1173–1183 (1980).
26. A. Papayannis, G. Ancellet, J. Pelon, and G. Mégie, "Multiwavelength lidar for ozone measurements in the troposphere and the lower stratosphere," Appl. Opt. **29,** 467–476 (1990).
27. G. Ancellet and F. Ravetta, "Compact airborne lidar for tropospheric ozone: description and field measurements," Appl. Opt. **37,** 5509–5521 (1998).
28. L. T. Molina and M. J. Molina, Absolute "Absorption cross sections of ozone in the 185 to 350 nm wavelength range," J. Geophys. Res. **91,** 14,501–14,508 (1986).
29. S. L. Valley, *Handbook of Geophysics and Space Environments, Atmospheric Optics* (McGraw-Hill, New York, 1965), Chap. 7, pp. 1–36.
30. D. B. Rensch and R. K. Long, "Comparative studies of extinction and backscattering by aerosols, fog, and rain at 10.6 and 0.63 μm," Appl. Opt. **9,** 1563–1573 (1970).
31. D. A. Haner and I. S. Mc Dermid, "Stimulated Raman shifting of the Nd:YAG fourth harmonic (266 nm) in H_2, HD and D_2," IEEE J. Quantum Electron. **26,** 1292–1298 (1990).
32. L. De Schoulepnikoff, V. Mitev, V. Simeonov, B. Calpini, and H. Van den Bergh, "Experimental investigation of high-power single pass Raman shifters in the ultraviolet with Nd:YAG and KrF lasers," Appl. Opt. **36,** 5026–5043 (1997).
33. T. Halldorsson and J. Langerholc, "Geometrical form factors for the lidar function," Appl. Opt. **17,** 240–244 (1978).
34. H. S. Lee, G. Schwemmer, C. Korb, M. Dombrowski, and C. Prasad, "Gated photomultiplier response characterization for DIAL measurements," Appl. Opt. **29,** 3303–3315 (1990).
35. R. M. Measure, *Laser Remote Sensing: Fundamentals and Applications* (Krieger, Malabar, Fla., 1992).
36. J. D. Klett, "Stable analytical inversion solution for processing lidar returns," Appl. Opt. **20,** 211–220 (1981).
37. J. D. Klett, "Lidar inversion with variable backscatter/extinction ratios," Appl. Opt. **24,** 1638–1643 (1985).
38. E. Browell, S. Ismail, and S. Shipley, "Ultraviolet DIAL measurements of O_3 profiles in regions of spatially inhomogeneous aerosols," Appl. Opt. **24,** 2827–2836 (1985).
39. V. A. Kovalev and J. L. McElroy, "Differential absorption lidar measurement of vertical ozone profiles in the troposphere that contains aerosol layers with strong backscattering gradients: a simplified version," Appl. Opt. **33,** 8393–8401 (1994).
40. A. M. Bass and R. J. Paur, "Ultraviolet absorption cross-section of ozone: measurements, results and error analysis," in *Proceedings, Quadriennal Ozone Symposium, Halkidiki, Greece* (Reidel, Hingham, Mass., 1984), p. 606.
41. A. M. Bass, A. E. Ledford, Jr., and A. H. Laufer, "Extinction coefficients of NO_2 and N_2O_4," J. Res. Natl. Bur. Stand. Sect. A **80,** 143–166 (1976).
42. S. L. Manatt and A. L. Lane, "A compilation of the absorption cross section of SO_2 from 106 to 403 nm," J. Quant. Spectrosc. Radiat. Transfer **50,** 267–276 (1993).
43. D. P. Donovan, J. A. Whiteway, and A. I. Carswell, "Correction for non-linear photon-counting effects in lidar systems," Appl. Opt. **32,** 6742–6753 (1993).
44. J. P. Thayer, N. B. Nielsen, R. E. Warren, C. J. Heinselman, and J. Sohn, "Rayleigh lidar system for middle atmosphere research in the Arctic," Opt. Eng. **36,** 2045–2061 (1997).
45. L. Fiorani, B. Calpini, L. Jaquet, H. Van den Bergh, and E. Dirieux, "Correction scheme for experimental biases in differential absorption lidar tropospheric ozone measurements based on the analysis of shot per shot data samples," Appl. Opt. **36,** 6857–6863 (1997).
46. R. A. Barnes, A. R. Bandy, and A. L. Torres, "Electrochemical concentration cell ozonesonde accuracy and precision," J. Geophys. Res. **90,** 7881–7888 (1985).